Contributed paper

OPTO-ELECTRONICS REVIEW **11**(1), 65–75 (2003)

Fully self-consistent three-dimensional model of edge-emitting nitride diode lasers

A. TOMCZYK[1], R.P. SARZAŁA[1], T. CZYSZANOWSKI[1], M. WASIAK[1], and W. NAKWASKI*[1,2]

[1]Institute of Physics, Technical University of Łódź, 219 Wólczańska Str., 93-005 Łódź, Poland
[2]Centre for High Technology Materials, University of New Mexico, Albuquerque, NM, USA

A comprehensive, fully self-consistent, optical-electrical-thermal-gain, three-dimensional model of edge-emitting (EE) nitride diode lasers has been developed and used to simulate a room-temperature (RT) continuous-wave (CW) threshold operation of typical EE designs of a nitride diode laser. With the aid of the model, some RT CW performance characteristics of the laser have been anticipated taking into consideration important features of nitride materials. These features have proved already to be often essentially different from those of other $A^{III}B^{V}$ materials, therefore expected properties of nitride devices cannot be estimated on the basis of known properties of analogous devices manufactured from other materials.

Keywords: nitride diode lasers, modelling of a diode-laser operation, edge-emitting diode lasers.

1. Introduction

Development of diode lasers initially has been based on arsenide lasers emitting in the near infrared part of the spectrum, usually in the first (0.85 μm) optical window of the fibre attenuation spectrum. Afterwards fibre optical communication has initiated interest in phosphide lasers, especially those emitting in the second (1.3 μm) and the third (1.55 μm) analogous windows. Recently, an expected increase in a recording density on optical discs as well as application in full-colour optical displays and under-water communication systems have started a true race of technological centres to manufacture reliable, high-performance nitride lasers emitting in blue, violet, and even ultraviolet parts of the spectrum.

Currently, an increasing number of technological centres are reporting manufacturing various designs of edge-emitting (EE) nitride diode lasers operating at room temperature (RT). There is still, however, a number of unsolved problems and unanswered questions associated with their possible structure optimisation. It is a direct consequence of the fact, that the physics of nitride devices often differs significantly from the physics of other $A^{III}B^{V}$ devices, therefore expected behaviours of novel nitride designs cannot be simply estimated on the basis of known properties of analogous designs manufactured from other $A^{III}B^{V}$ materials. Performance characteristics of proposed nitride devices can be, however, anticipated with the aid of a detailed physical simulation taking into account all important features of nitride materials. Therefore the main goal of this work is to develop a comprehensive, fully self-consistent threshold optical-electrical-thermal-gain three-dimensional (3D) model of EE nitride diode lasers taking into account all important features of nitride materials. Both index-guided (IG) and gain-guided (GG) structures of nitride EE diode lasers are considered. The model is intended to be used to better understand interactions between individual physical processes governing a laser operation, to simulate expected performance characteristics of nitride EE diode lasers, and to optimise their structures for specified applications.

In the present paper, the model and its first simulation results are presented. The paper is organised as follows. The model is shortly explained in Section 2. Both IG and GG designs of the laser under consideration are shown in Section 3. First results of a simulation of an operation of nitride EE diode laser designs are discussed in Section 4, which is followed by conclusion in Section 5.

2. Model

The model is composed of four interrelated parts describing optical, electrical, thermal, and gain physical phenomena [1–4]. Below, the above-mentioned submodels will be shortly described together with important interactions between them. The co-ordinate system is shown in Fig. 1.

2.1. Optical model

Behaviour of an optical field within the laser resonator is described in this work with the aid of the method of lines (MoL) [5], a semi-analytical fully vectorial optical ap-

*e-mail: nakwaski@ck-sg.p.lodz.pl

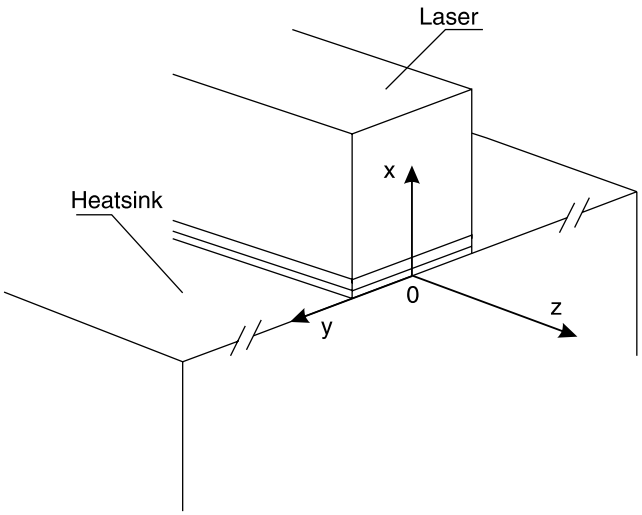

Fig. 1. The co-ordinate system.

proach. We decided not to use much simpler scalar optical approaches (for example the effective index method) because their exactness is supposed to be reduced with an anticipated decrease in transversal sizes of the laser resonator. Using MoL, along the 0*x* axial direction perpendicular to the p-n junction plane (see Fig. 1), the laser structure is assumed to be divided into layers of constant material parameters. MoL allows, however, lateral (along the 0*y* axis) and longitudinal (along the 0*z* axis) dependences of refractive indices, carrier concentrations, optical gain and temperature to be included. In the method, discretisation is performed as far as it is necessary whereas an analytical procedure is used elsewhere. This enables obtaining accurate results with less computational effort than in case of other fully vectorial techniques as the finite element method or the finite difference method. What is more, the MoL approach has no problems with the relative convergence behaviour. Non-physical or spurious modes do not appear in MoL. Besides, it makes possible analysis of structures with expected small transversal sizes.

Optical properties of the structure are described with the aid of the complex index of refraction N_R

$$N_R(x,y,z) = n_R(x,y,z) - ik_e(x,y,z), \tag{1}$$

where n_R stands for the 3D profile of an index of refraction and k_e is the analogous 3D profile of an extinction coefficient directly associated with the absorption coefficient α (which may change its sign becoming the optical gain g in an active region)

$$k_e = \frac{\lambda}{2\pi}\alpha, \tag{2}$$

Both (real and imaginary) parts of N_R are position-, temperature- and carrier-concentration-dependent values, therefore their actual 3D profiles should be recalculated in each algorithm loop taking into account not only the layered laser structure, but also actual 3D profiles of temperature and carrier densities. Both refractive indices and extinction coefficients of structure layers of a RT threshold-operating diode laser are listed in Table 1. Different values of extinction coefficients of successive quantum

Table 1. Compositions, functions, thicknesses and doping levels of all structure layers as well as their refractive indices and extinction coefficients determined for the RT threshold-operating device.

Layer	Function	Thickness (μm)	Doping (cm^{-3})	Ref.	Refractive index	Extinction coefficient	Ref.
SiO_2	Oxide	0.5	0	–	1.560	0	[25]
p-GaN	Contacting	0.05	1×10^{18}	[23]	2.561	6.303×10^{-5}	[26]
p-$Al_{0.07}Ga_{0.93}N$	Confining	0.5	3×10^{17}	[23]	2.535	3.024×10^{-5}	[26]
p-GaN	Waveguide	0.1	3×10^{17}	[23]	2.561	3.024×10^{-5}	[26]
p-$Al_{0.19}Ga_{0.81}N$	Blocking	0.02	3×10^{17}	[23]	2.498	3.024×10^{-5}	[26]
$In_{0.20}Ga_{0.80}N$	Quantum well	0.003	2×10^{17}	[24]	2.569	0.008386	[26]
$In_{0.05}Ga_{0.95}N$	Barrier	0.005	2×10^{17}	[24]	2.675	0.0002748	[26]
$In_{0.20}Ga_{0.80}N$	Quantum well	0.003	2×10^{17}	[24]	2.569	–0.003661	[26]
$In_{0.05}Ga_{0.95}N$	Barrier	0.005	2×10^{17}	[24]	2.675	0.0002748	[26]
$In_{0.20}Ga_{0.80}N$	Quantum well	0.003	2×10^{17}	[24]	2.569	–0.01334	[26]
n-GaN	Waveguide	0.1	4.7×10^{16}	[11]	2.561	1.397×10^{-5}	[26]
n-$Al_{0.07}Ga_{0.93}N$	Confining	1	1×10^{18}	[23]	2.535	6.303×10^{-5}	[26]
n-GaN	Substrate	100	5×10^{17}	[8]	2.561	0.1598	[26]

wells (QWs) follows from their different injection levels. In particular, as one can see, within the first and the second QWs (but not within the third one), there exists optical gain instead of absorption. Relatively high value of an absorption within the substrate n-GaN layer follows from its poorer crystal quality than that of next structure levels.

The solution is looked for in an analytical form along the 0*x* axial direction, whereas the structure is discretised along the 0*y* direction. The *y* derivatives in the wave equation are replaced with appropriate difference operators, which yield the set of coupled ordinary differential equations [6]. The above equations have to be orthogonalised. The general solution is assumed in a form of a superposition of exponential functions. Finally, for the optical field of the *m*-th mode within the *j*-th layer, one obtains the following decoupled equation system

$$\frac{d^2}{dx^2}\overline{\Psi}_{j,m} - k_{x,j,m}^2\overline{\Psi}_{j,m} = 0, \tag{3}$$

with the analytical solution

$$\overline{\Psi}_{j,m} = A_{j,m}\cos h[k_{x,j,m}(x - x_j)] + B_{j,m}\sin h[k_{x,j,m}(x - x_j)], \tag{4}$$

where $\overline{\Psi}_{j,m}$ stands for the optical field transformation to principle axis whereas $k_{x,j,m}$ are propagation constants of successive modes in the 0*x* direction. The solution must satisfy the Helmholz equation and the Sturm-Lieuville equation. The threshold condition may be determined for each mode from the condition of its real propagation constant. The original field is obtained by an inverse transformation [7]. More about the solving algorithm may be found in Refs. 5–7.

2.2. Electrical model

For the continuous-wave (CW) room-temperature (RT) threshold laser operation considered here, the electrical model is composed of the Laplace equation

$$div\{\sigma(x,y,z)grad[V(x,y,z)]\} = 0, \tag{5}$$

and the diffusion equation within the active region

$$D(T)\frac{d^2 n_A(y)}{dy^2} - [An_A(y) + B(n_A,T)n_A^2(y) + Cn_A^3(y)] + \frac{j_{pn}(y)}{ed_A} = 0 \tag{6}$$

In the above equations, σ stands for the 3D electrical conductivity profile, *V* is the 3D potential distribution, *D* is the temperature-dependent ambipolar diffusion constant, n_A is the active-region carrier-concentration distribution, *A*, *B*, and *C* are the monomolecular, the bimolecular (mostly radiative), and the Auger, respectively, recombination coefficients, j_{pn} (*y*) stands for the p-n junction current-density distribution, *e* is the electron charge, and d_A is the cumulative active-region thickness. The Laplace equation, instead of the Poisson one, is used because non-compensated electric charges are confined only to the active-region area, which is treated separately [4].

3D current-density profiles are calculated from the potential distribution using the Ohm's law

$$j(x,y,z) = \sigma(x,y,z)grad[V(x,y,z)], \tag{7}$$

where electrical conductivity profiles σ(*x*,*y*,*z*) are determined from the relation

$$\sigma(x,y,z) = en[T(x,y,z),x,y,z]\mu[T(x,y,z),x,y,z], \tag{8}$$

everywhere with an exception of the active region, where its effective σ_{pn} value is found with the aid of a measured current-voltage characteristic

$$j_{pn} = j_s[\exp(\beta_{pn}U_{pn}) - 1], \tag{9}$$

in a following form

$$\sigma_{pn}(y) = \frac{\beta_{pn}j_{pn}(y)d_A}{\ln\left(\frac{j_{pn}(y)}{j_s} + 1\right)}. \tag{10}$$

From the experimental characteristics reported for the reference laser design (c.f. Section 3) in [8], β_{pn} = 3.98945 V^{-1} and j_s = 0.109 A/cm^2 values have been extracted. In the above equations, μ stands for the 3D distribution of the carrier mobility, *T* is the 3D temperature profile, j_s is the saturation reverse current density, U_{pn} is the voltage drop at the p-n junction, and β_{pn} may be expressed in a following form

$$\beta_{pn} = \frac{e}{m_{pn}k_B T}, \tag{11}$$

where m_{pn} is the ideality factor and k_B stands for the Boltzmann constant.

Doping- and temperature-dependent values of mobilities and carrier concentrations of Si-doped and Mg-doped GaN layers have been determined on the basis of measurements reported by Kuramato *et al.* [8] and Götz *et al.* [9] and sometimes using empirical formulae proposed by Maćkowiak and Nakwaski [10]. Empirical relations given in Ref. 10 have been also used to determine composition-, doping-, and temperature-dependent values of electrical resistivities of analogous $Al_xGa_{1-x}N$ layers, whereas their values for non-intentionally doped GaN have been found in Refs. 11 and 12. For the copper radiator and SiO_2 areas, RT electrical-resistivities were assumed to be 1.7×10^{-6} Ω cm [13] and 10^{18} Ω cm [14], respectively. Room-temperature

values of electrical resitivities used in our simulation are listed in Table 2. Surprisingly high resistivity of the n-type GaN waveguide layer (even higher than that of the p-type one) follows from its extremely low doping (c.f. Table 1). For the n-side (titanium and aluminium) and the p-side (palladium, platinum, and gold) contact layers, contact resistances of 4.63×10^{-4} $\Omega\,cm^2$ [15] and 10^{-5} $\Omega\,cm^2$ [16], respectively, have been found.

Table 2. Room-temperature values of electrical resistivities.

Layer	Resistivity (Ω cm)
SiO_2	10^{18}
Copper radiator	1.7×10^{-6}
p-side contact	20
p-GaN contact layer	0.207
p-$Al_{0.07}Ga_{0.93}N$ confinement layer	5.66
p-GaN waveguide layer	1.2
p-$Al_{0.19}Ga_{0.81}N$ blocking layer	200
n-GaN waveguide layer	1.725
n-$Al_{0.07}Ga_{0.93}N$ confinement layer	0.0246
n-GaN substrate	0.0614
n-side contact	9.276

Taking advantage of the analysis reported in Ref. 10, the monomolecular-recombination coefficient $A = 10^8$ s^{-1}, the Auger-recombination coefficient $C = 1.5\times10^{-30}$ cm^6s^{-1}, and the temperature-dependent diffusion constant $D = 10(T/300\ K)$ cm^2s^{-1} are used. From analysis reported by Dmitriev and Oruzheinikov [17], the carrier-concentration-dependent bimolecular recombination coefficient B may be for nitride lasers written in the following way

$$B(n) = \frac{4.78\times10^{-11}\,cm^3s^{-1}}{\left(1+\dfrac{n}{2.1\times10^{19}\,cm^{-3}}\right)^{0.96}}. \tag{12}$$

2.3. Thermal model

Temperature 3D profiles are found in the laser structure using the thermal conduction equation

$$\begin{aligned} &div\{k[T(x,y,z),x,y,z]\cdot grad[T(x,y,z)]\} = \\ &= -g_T[T(x,y,z),x,y,z] \end{aligned}, \tag{13}$$

with the temperature- and position-dependent thermal conductivity k. g_T stands for the 3D distribution of heat generation (in Wm^{-3}).

Heat sinking in the (5×5 mm^2) copper radiator is properly taken into account assuming its much larger dimensions than those of the laser crystal, so its external walls are assumed to remain at RT of the ambient. Top and side-walls of the laser crystal are assumed to be thermally isolated because of negligible effect of thermal radiation and thermal diffusion of air particles.

The following heat sources are considered:

- non-radiative recombination and re-absorption of spontaneous radiation within the active region,
- barrier Joule heating in both electric contacts,
- volume Joule heating in all structure layers.

For binary GaN and AlN compounds, the values of the RT thermal conductivities are found in [18] and their relative temperature dependences are extracted from data published in Ref. 19, giving finally (in $Wm^{-1}K^{-1}$)

$$k_{GaN}(T) = 130\left(\frac{300K}{T}\right)^{0.2635}, \tag{14}$$

$$k_{AlN} = 200 - 0.247(T - 300K). \tag{15}$$

To the best of the authors' knowledge, there are no published measurements of thermal conductivities in ternary $Al_xGa_{1-x}N$ compounds. Therefore following the approach proposed in Ref. 20 and the analysis reported in Ref. 10, the following relation is used for temperature- and composition-dependent thermal conductivity of $Al_xGa_{1-x}N$ (in $Wm^{-1}K^{-1}$)

$$\begin{aligned} k_{AlGaN}(T) = \{&x[k_{GaN}(T)]^{-1} + (1-x)[k_{AlN}(T)]^{-1} + \\ &+ 0.05x(1-x)\}^{-1} \end{aligned}. \tag{16}$$

Thermal conductivities of SiO_2 was found to be equal to 1.38 W/mK [21] and that for the copper radiator – 398 W/mK [21]. Effective thermal conductivity of a two-layer contact is calculated using the relation

$$k_{AB} = \frac{k_Ak_B(d_A + d_B)}{d_Ak_B + d_Bk_A}, \tag{17}$$

where k_A, k_B and d_A, d_B are the thermal conductivities and the thicknesses, respectively, of both constituent A and B layers. For a three-layer contact, this approach should be repeated. Using the following values of thermal conductivities [21] of the contact materials: $k_{Ti} = 22$ W/mK, $k_{Al} = 237$ W/mK, $k_{Pd} = 72$ W/mK, $k_{Pt} = 72$ W/mK, and $k_{Au} = 317$ W/mK, the thermal conductivity of the p-side Ti (35 nm)/Al (300 nm) contact has been determined to be equal to 132 W/mK, and that of the n-side Pd (20 nm)/Pt (50 nm)/Au (100 nm) contact – 117 W/mK.

2.4. Gain model

In the calculations of the optical gain in nitride quantum wells, the classical Fermi's golden rule, the parabolic band-gap approximation and the Lorentzian broadening mechanism are assumed [2]. The optical gain spectra g may be then determined from the following relation

$$g(\hbar\omega) = \sum_m \int_{-\infty}^{\infty} g_m(\varepsilon)\Lambda(\hbar\omega - \varepsilon)d\varepsilon, \tag{18}$$

where the summation should be carried out over all available numbers m of level pairs and

$$g_m(\hbar\omega) = \frac{e^2\pi\hbar}{n_R c m_0^2 \varepsilon_0}\frac{M^2\rho_r^{2D}(\hbar\omega)}{\hbar\omega}, \tag{19}$$
$$\times\{f_c[E_e(m,\hbar\omega)] - f_v[E_h(m,\hbar\omega)]\}$$

where n_R stands for the index of refraction, c is the speed of light in vacuum, m_0 is the electron rest mass, ε_0 is the vacuum dielectric constant, M is the momentum matrix element, ρ_r^{2D} stands for the two-dimensional reduced density of states, f_c and f_v are the Fermi-Dirac functions determined for electrons in the conduction band and for holes in the valence band, respectively, E_e and E_h are energies of the recombining electron and hole, respectively, and Λ is the broadening function [22], usually of the Lorentzian type. Values of parameters used to determine gain spectra are listed in Table 3.

3. Laser structure

The model has been applied to simulate an operation of the index-guided (IG) structure of the EE nitride diode laser [shown in Fig. 2(a)] reported by Kuramato *et al*. [8]. The wavelength of an emitted radiation was equal to 401.5 nm. Compositions, functions, thicknesses and doping levels of successive structure layers are listed in Table 1. This high-performance design has been chosen for our analysis because it enables manufacturing one-dimensional laser arrays which are intended to be considered in our next paper. As compared with other designs of nitride EE diode lasers, the main feature of this laser is connected with localisation of its n-side contact, which has been fabricated on the bottom surface of the n-GaN substrate. Such a contact configuration ensures much more uniform current injection into the laser active region than in laser structures with both contacts localized on the same side of the laser crystal. Besides, the laser structure considered in this paper enables application its 'upside-down' (p-side down) configuration, when the laser is attached to the copper radiator on its p-type side. This configuration enhances considerably heat-sinking process, therefore it is highly recommended for CW-operated lasers.

The multiple-quantum-well (MQW) active region is composed of three 3-nm $In_{0.2}Ga_{0.8}N$ QWs separated with two 5-nm $In_{0.05}Ga_{0.95}N$ barriers. 20-nm p-type $Al_{0.19}Ga_{0.81}N$ current blocking/carrier confinement layer is confining the active region on its p-type side. This structure is sandwiched by two 0.1-μm p-type and n-type GaN waveguide layers and two 0.5-μm p-type and 1-μm n-type $Al_{0.07}Ga_{0.93}N$ confining layers. The upper 0.05-μm GaN layer ensures low electrical resistivity of the upper contact beyond the insulating 0.5-μm SiO_2 layer. The bottom

Table 3. Parameters used to determine gain spectra.

Index of refraction of the quantum-well material	2.55
Energy gap of the quantum-well material	2.948 eV
Quantum-well width	30 Å
Waveguide width	2390 Å
Quantum-well depth in the conduction band	0.208 eV
Quantum-well depth in the valence band	0.138 eV
Waveguide depth in the conduction band	0.075 eV
Waveguide depth in the valence band	0.050 eV
Electron effective mass in the p-n junction plane	0.168 m
Electron effective mass in the direction perpendicular to the p-n junction plane	0.187 m
Heavy-hole effective mass in the p-n junction plane	1.635 m_0
Heavy-hole effective mass in the direction perpendicular to the p-n junction plane	1.158 m_0
Electron effective mass in the barrier	0.185 m_0
Heavy-hole effective mass in the barrier	1.412 m_0
Light-hole effective mass in the barrier	0.196 m_0
Momentum matrix element	6.408 m_0 eV
Electron lifetime with respect to the stimulated emission	0.1 ps

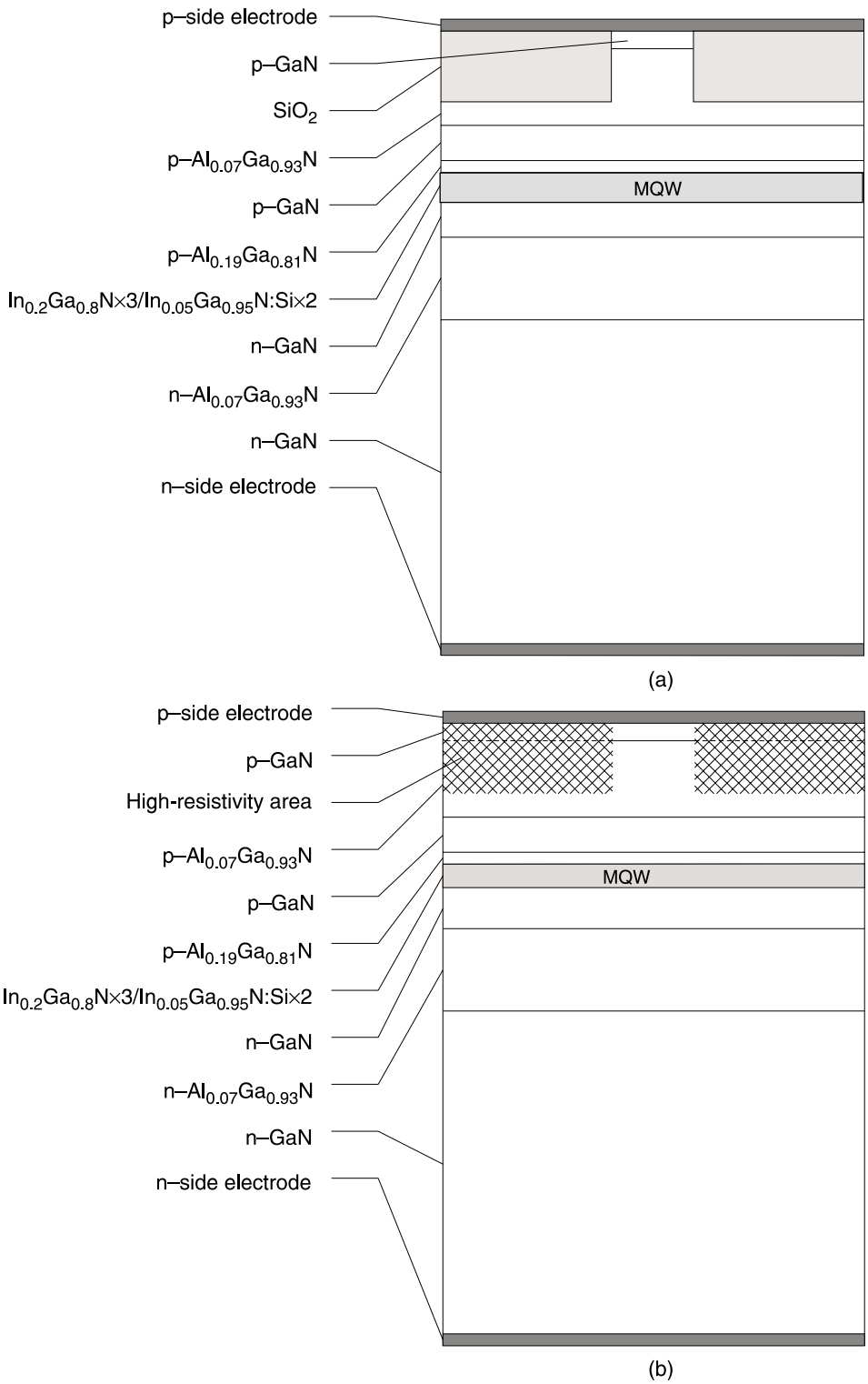

Fig. 2. Schematic structures of the nitride diode laser used in the calculations: (a) the IG nitride laser, (b) the GG nitride laser.

100-μm GaN substrate layer is adjoining the bottom contact. The laser is attached to the copper radiator (heat sink).

The laser is equipped with the ridge waveguide of the width equal to 3 μm. Reflectivity of the rear resonant mirror has been increased up to 93% with the aid of the four-period TiO_2/SiO_2 distributed Bragg reflectors. Resonator length is equal to 440 μm. To attach the ridge-side of the p-side-down laser to the radiator, SiO_2 is used to fill all empty spaces [Fig. 2(a)]. The normal p-side-up IG laser configuration is also analysed.

The second laser structure to be considered is the gain-guided (GG) nitride EE diode laser [Fig. 2(b)]. As

compared to the IG nitride laser considered here [Fig. 2(a)], its IG ridge structure is replaced in the GG laser with high-resistivity areas confining the stripe active region in the p-n junction plane. Their high resistivity may be obtained using for example $^2H^+$ ion implantation. This design is proposed on the basis on analogous arsenide laser designs.

4. Results

The self-consistent model developed in this paper has been applied to simulate threshold RT CW operation of the designs of nitride EE diode lasers presented in Section 3. Results of this simulation are shown in successive figures.

4.1. Thermal properties

The p-side-down configuration of the IG diode laser has been found to exhibit very good thermal properties. Thanks to relatively short distance between its active region and the copper radiator, the active-region temperature increase at RT CW lasing threshold is equal to only about 21 K (Fig. 3) over the ambient RT. Heat spreading inside the radiator is very efficient. It is distinctly the 3D spreading, because isotherm lines compose practically semispheres with their central point located inside the active region. 3D heat-flux spreading is also seen within a lower part of the laser crystal. Heat fluxes are there initially flowing radially in all directions, but afterwards they are gradually changing their directions towards the radiator. In the middle and the upper parts of the laser crystal, distinctly one-dimensional (1D) heat-flux flow towards the radiator can be observed. It is interesting to note, that temperature of the top surface of

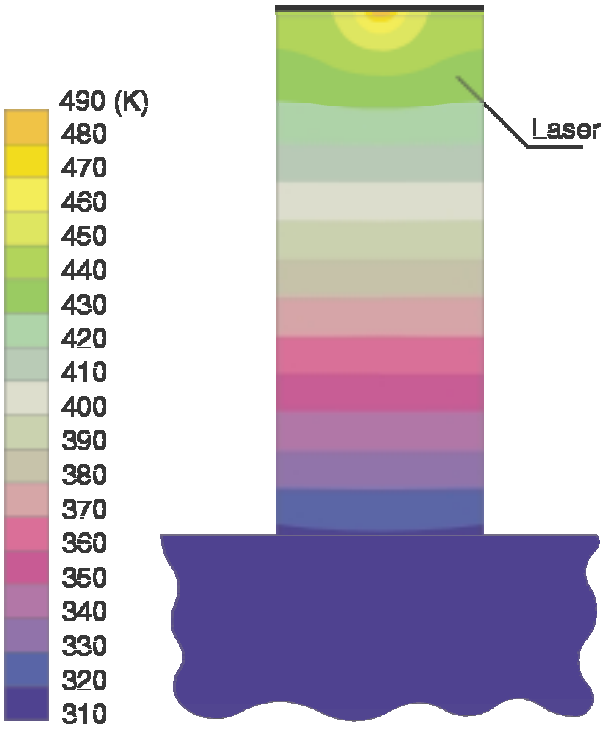

Fig. 4. Temperature 2D profile within a volume of RT CW threshold-operated nitride IG diode laser of the normal 'p-side-up' (n-side-down) configuration.

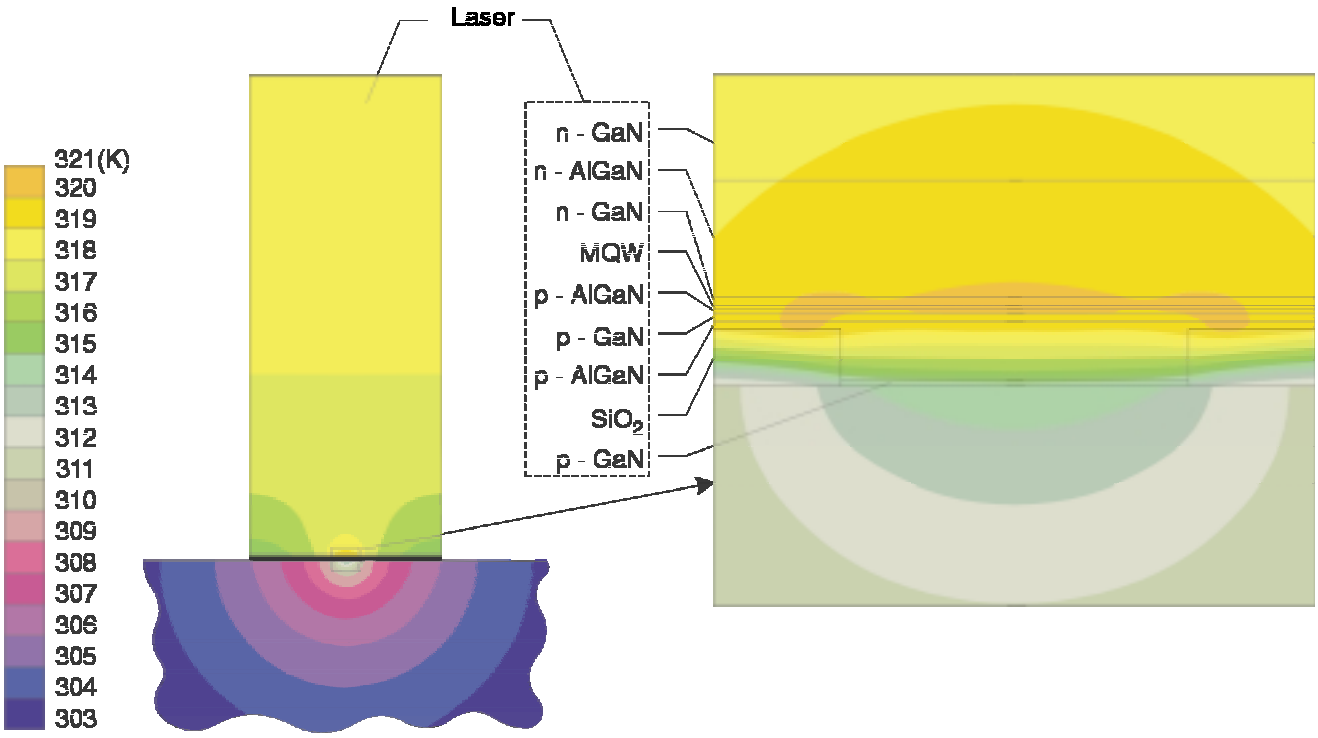

Fig. 3. Temperature 2D profile within a volume of RT CW threshold-operated nitride IG diode laser of the 'upside-down' (p-side down) configuration.

the laser crystal is in this case lower only by about 2 K than that within the active region. There are two reasons of such a behaviour. The first is associated with a very efficient heat abstraction process from the active region. The second is a result of intense heat sources located outside the active region, e.g., the volume Joule heating within the layers located over it and the barrier Joule heating at the upper contact.

It is interesting to compare the above advantageous thermal properties of the p-side-down laser configuration with those of the n-side-down (p-side-up) one. As it can be seen in Fig. 4, the active region is again at the highest temperature, but this time its temperature increase over RT is as high as 190 K. It is definitely too much to ensure efficient and reliable operation of a nitride diode laser. Heat flux spreading is three-dimensional only just beneath the active region. Efficiency of the heat abstraction within the high-thermal-conductivity copper heat sink is practically meaningless.

The GG structure of the nitride diode laser seems to have even better thermal properties than the IG one because low-thermal-conductivity SiO_2 areas have been replaced here with semiconductor areas of much higher thermal conductivities. Nevertheless, the highest active-region temperature increase (Fig. 5) over RT determined in this case (53 K) has been found to be much higher than that in the IG laser. The reason of this is associated with optical properties of the GG laser, strictly speaking, with its much higher RT CW lasing threshold, which will be analysed later.

4.2. Electrical properties

The axial potential profile within the IG p-side-down nitride EE diode laser for its RT CW lasing-threshold condition is plotted in Fig. 6. As expected, the highest potential increase is observed within the active region and the p-$Al_{0.19}Ga_{0.81}N$ blocking layer. Distinct potential changes can be also seen within the p-$Al_{0.07}Ga_{0.93}N$ confinement layer, whereas lower changes are within both the waveguide p-GaN and the n-GaN layers. Analogous axial profile determined for the GG laser is very similar but with higher potential changes: the RT CW threshold values of a supply voltage are equal to 10.50 V for the IG laser and to 14.44 V – for the GG one. Potential profiles within the IG laser are plotted in Fig. 7.

In the successive two figures, the RT CW threshold current density profiles (Fig. 8) and the RT CW threshold carrier concentration profiles (Fig. 9) are plotted for both the IG and the GG p-side-down nitride designs. All of these plots exhibit classical bell-like behaviours with some tails penetrating lateral passive areas. Lower values of both plots corresponding to the IG laser are associated with its lower lasing threshold. As one can see, current injection is

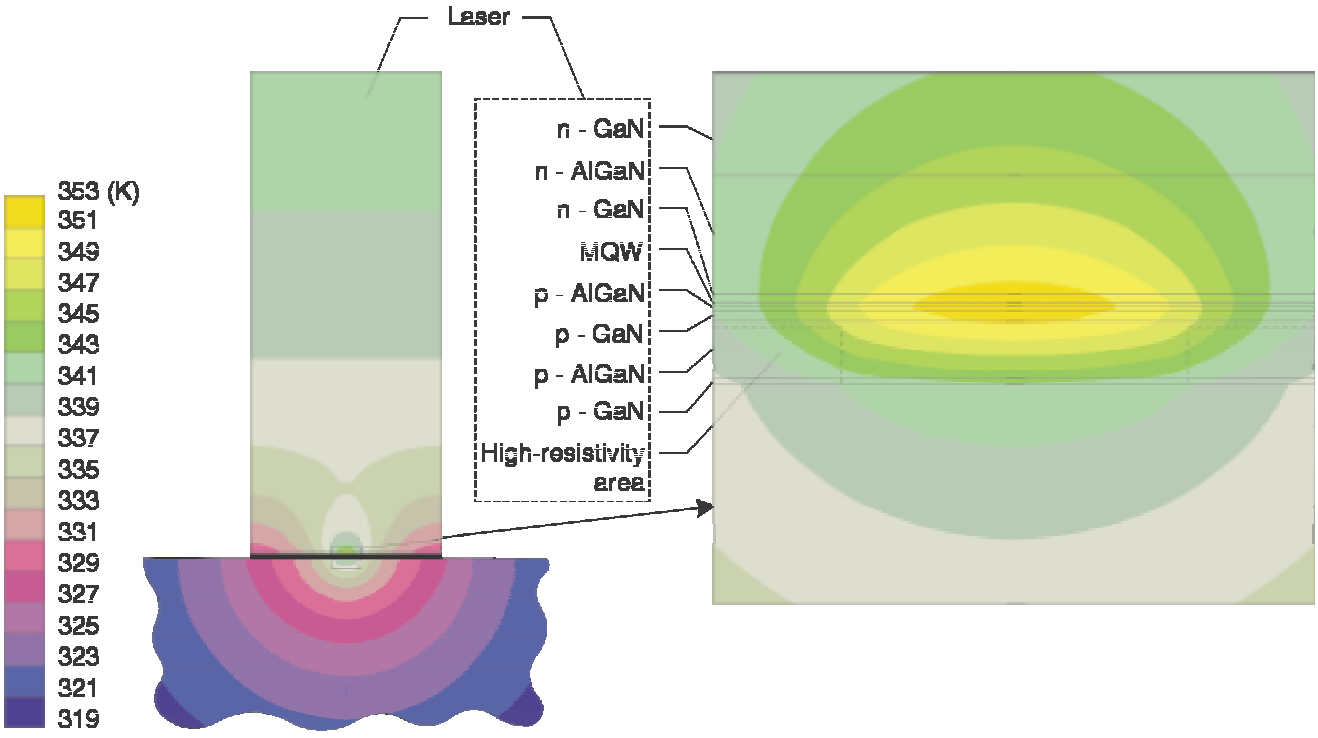

Fig. 5. Temperature 2D profile within a volume of RT CW threshold-operated nitride GG diode laser of the 'upside-down' configuration.

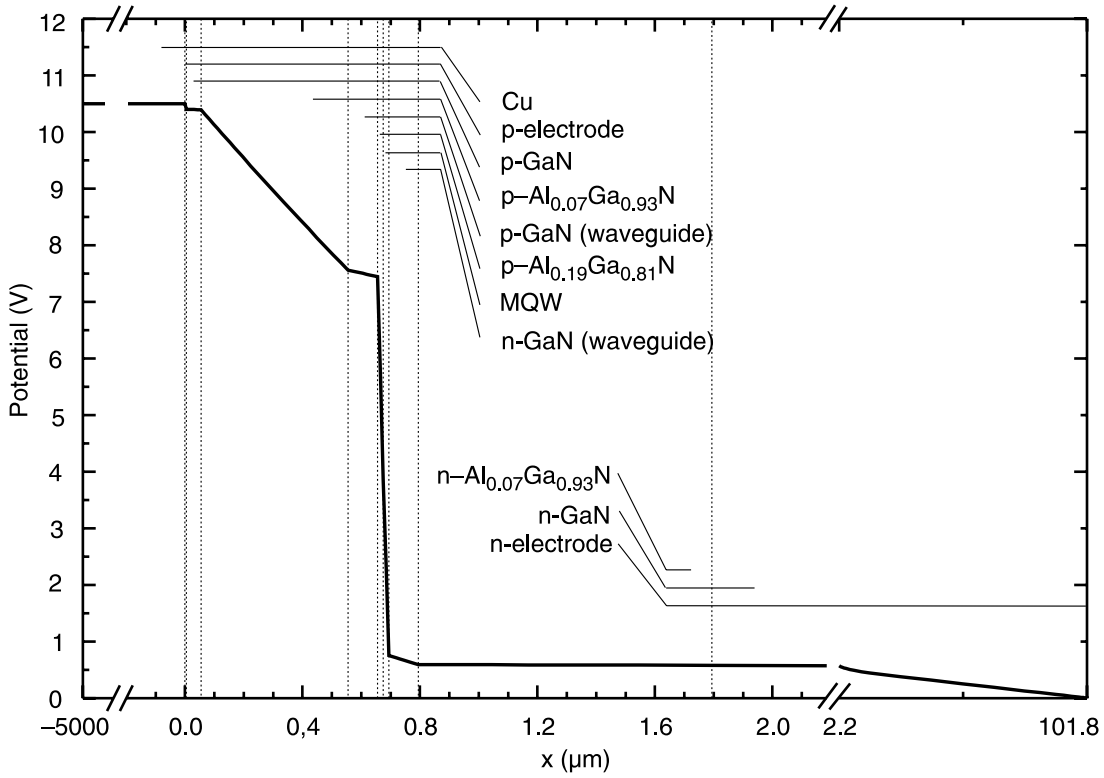

Fig. 6. Axial (along the *x* axis) potential profile within the RT CW threshold-operating IG EE nitride diode laser.

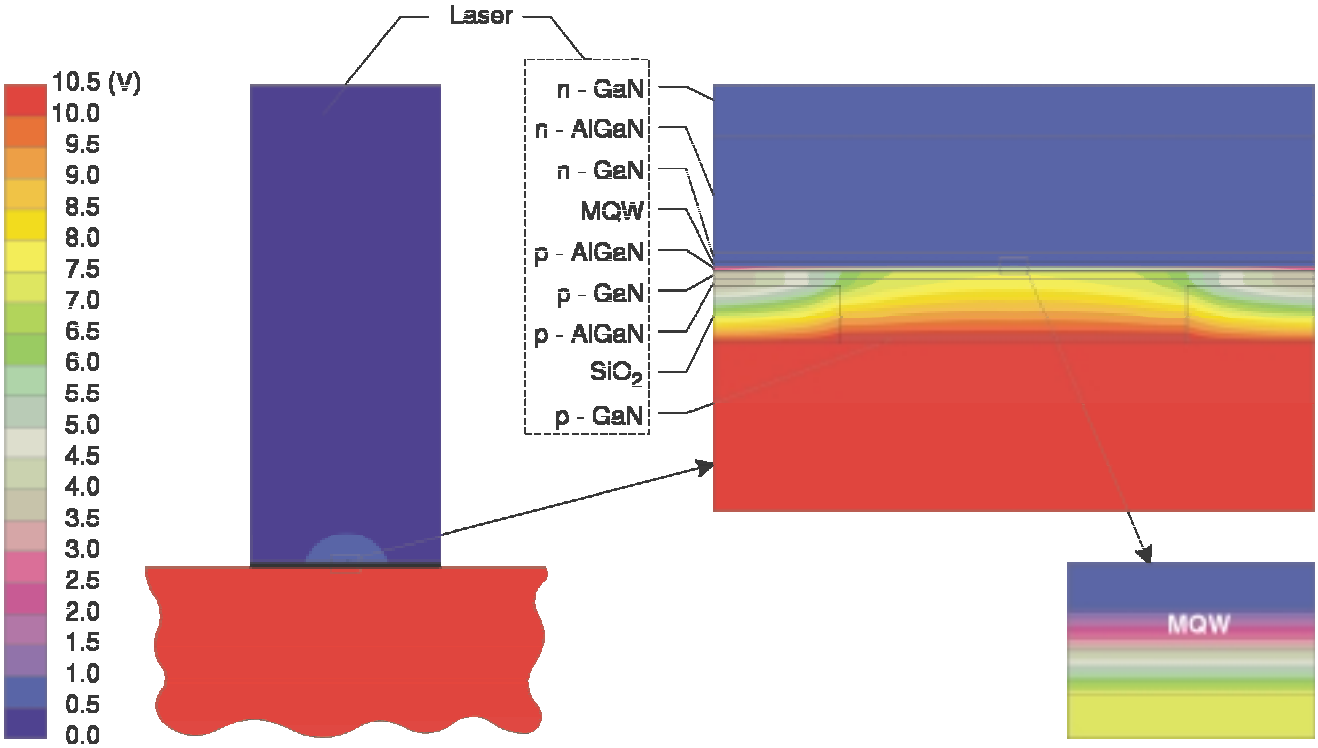

Fig. 7. Potential 2D profile within a volume of RT CW threshold-operated nitride IG diode laser of the 'upside-down' configuration.

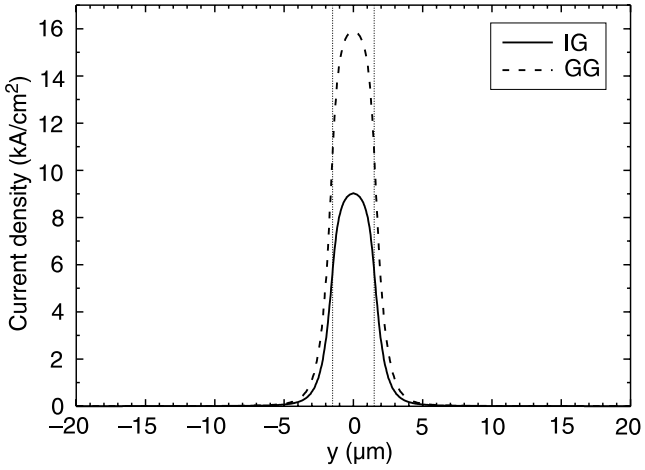

Fig. 8. RT CW threshold p-n junction current-density profiles of nitride IG and GG diode lasers of the 'upside-down' configuration along the 0*y* axis.

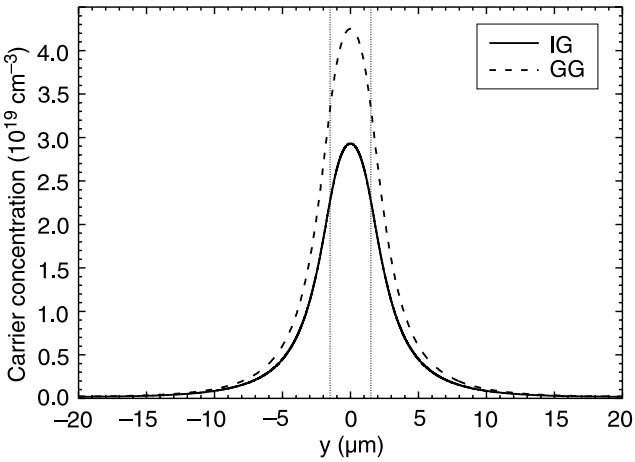

Fig. 9. RT CW threshold active-region carrier-concentration profiles of nitride IG and GG diode lasers of the 'upside-down' configuration along the 0*y* axis.

confined to narrower stripes than carrier concentration which follows from an additional lateral carrier diffusion before their recombination.

4.3. Optical properties

3D active-region intensity profiles of the most desired fundamental TE_{00} mode in both the IG and the GG designs of the p-side-down (upside-down) EE nitride diode laser under consideration during their RT CW threshold operation are plotted in Fig. 10. The most essential difference between them is associated with much more intense penetration lateral passive areas by an optical field in the case of the GG laser. In both laser designs, the active region is 3 μm wide. It may be seen in Fig. 10, that the TE_{00} optical field is very well confined within the active region of the IG laser whereas it is spread to much wider area in the GG one. This has turned out to be the main reason of a distinctly higher threshold of the latter laser design because of additional optical losses in its lateral passive areas which requires higher carrier concentrations (and higher operation current) within its active region to be compensated.

5. Conclusions

The comprehensive three-dimensional fully self-consistent optical-electrical-thermal-gain model of nitride edge-emitting (EE) diode lasers has been developed and applied to simulate their room-temperature (RT) continuous-wave (CW) threshold operation. The 'upside-down' (p-side-down) laser configuration has been found to exhibit distinctly better thermal properties than the n-side-down (p-side-up) one. Therefore lasers of the former design are recommended for their RT CW operation as well as for their possible integration into one-dimensional laser arrays. The index-guided (IG) design of nitride EE diode lasers has

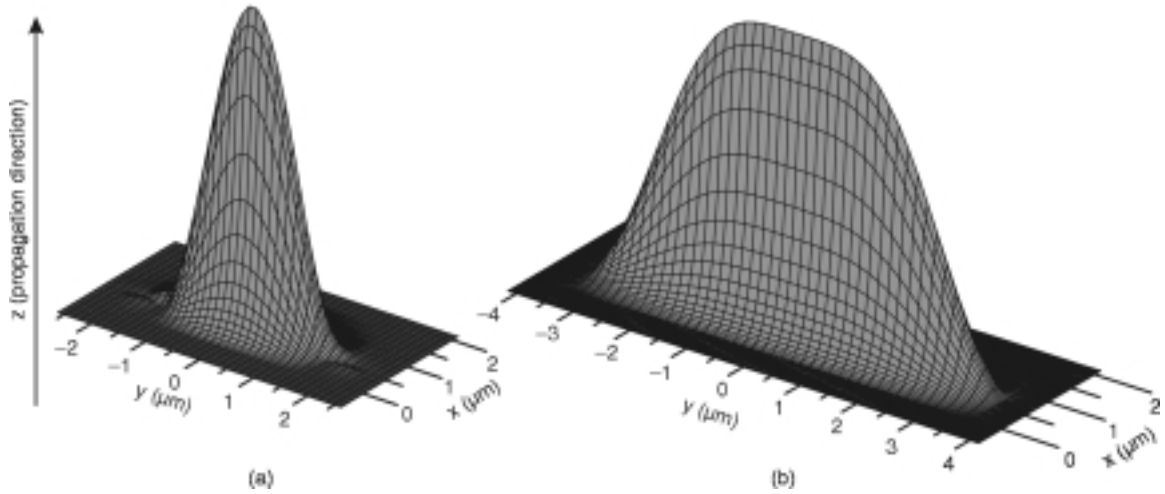

Fig. 10. 3D active-region intensity profiles of the fundamental TE_{00} mode determined for the threshold RT CW operation of the nitride EE diode lasers of (a) the IG configuration,(b) the GG configuration.

been determined to demonstrate definitely lower RT CW lasing thresholds than the gain-guided (GG) one because, in GG lasers, a considerable penetration of passive lateral areas by the laser radiation is followed by its increasing absorption losses. Therefore IG nitride EE diode lasers have been found to be better candidates as emitters in possible one-dimensional arrays of nitride diode lasers than their GG counterparts. This conclusion is valid even taking into consideration distinctly worse thermal properties of IG lasers followed from extremely low thermal conductivities of their lateral SiO_2 layers.

Acknowledgements

This work was supported by the EU under the IST Programme ('GSQ' project) and by the Polish State Committee for Scientific Research (KBN), grant No 7-T11B-073-21.

References

1. B. Mroziewicz, M. Bugajski, and W. Nakwaski, *Physics of Semiconductor Lasers*, North-Holland Science Publishers B.V. & Polish Scientific Publishers – PWN, Amsterdam/ /Warsaw 1991.
2. S.L. Chuang, *Physics of Optoelectronics Devices*, John Wiley & Sons, New York 1995.
3. W. Nakwaski, "Simulation of optical phenomena in vertical-cavity surface-emitting lasers, I. Fundamental principles, II. Models", *Opto-Electron. Rev.* **8**, 11 and 19 (2000).
4. M. Osiński and W. Nakwaski, "Three-dimensional simulation of vertical-cavity surface-emitting semiconductor lasers", Chapter 5 in *Vertical-Cavity Surface-Emitting Laser Devices*, pp. 135–192, edited by H. Li and K. Iga, Springer Verlag, Berlin 2003.
5. O. Conradi, S. Helfert, and R. Pregla, "Comprehensive modelling of vertical-cavity laser-diodes by the method of lines", *IEEE J. Quantum Electron.* **37**, 928 (2001).
6. R. Pregla and W. Pasher, "The method of lines", Chapter 6 in *Numerical Techniques for Microwave and Millimeter Wave Passive Structures*, pp. 381–446, edited by T. Itoh, John Wiley & Sons, New York 1989.
7. S.F. Helfert and R. Pregla, "Efficient analysis of periodic structures", *J. Lightwave Technol.* **16**, 1694 (1998).
8. M. Kuramato, C. Sasaoka, Y. Hisanaga, A. Kimura, A.A. Yamaguchi, H. Sunakawa, N. Kuroda, M. Nido, A. Usui, and M. Mizuta, "Room-temperature continuous-wave operation of InGaN multi-quantum-well laser diodes grown on an n-GaN substrate with a backside n-contact", *Jpn. J. Appl. Phys.* **35**, Part 2, L184 (1999).
9. W. Götz, N.M. Johnson, C. Chen, H. Liu, C. Kuo, and W. Imler, "Activation energies of Si donors in GaN", *Appl. Phys. Lett.* **68**, 3144 (1996).
10. P. Maćkowiak and W. Nakwaski, "Designing guidelines for possible continuous-wave-operating nitride vertical-cavity surface-emitting lasers", *J. Phys. D: Appl. Phys.* **33**, 642 (2000).
11. H.M. Chung, Y.C. Pau, W.C. Chung, N C. Chen, C.C. Tsai, C.I. Chiang, C.H. Liu, W. Chang, M.C. Lee, W.H. Chen, and W.K. Chen, "Long-term photocapacitance decay behaviour in undoped GaN", *Proc. Intern. Workshop on Nitride Semiconductors*, Nagoya (Japan) 24-27 Sept. 2000, IPAP Conf. Series **1** 463 (2000).
12. J.K. Shen, G.C. Chi, and M.J. Jou, "Improved electrical property of InGaN/GaN light-emitting diodes by using a Mg-doped AlGaN/GaN superlattices", *ibid*, **1** 856 (2000).
13. http://www.webelements.com/webelements/elements/ /text/Cu/phys.html
http://home.san.rr.com/nessengr/techdata/metalresist.html
14. E.M. Rabinovich, "Ceramic materials for electronic packaging", *Trans ASME, J. Electronic Packaging* **111**, 183 (1989).
15. E.F. Chor, D. Zhang, H. Gong, G.L. Chen, and T.Y.F. Liew, "Electrical characterisation and metallurgical analysis of Pd-containing multilayer contacts on GaN", *J. Appl. Phys.* **90**, 1242 (2001).
16. L.Ch Chien, J.K. Ho, Ch.Sh. Jong, Ch.C. Chiu, K.K. Shih, F.R. Chen, J.J. Kai, and L. Chang, "Oxidised Ni/Pt and Ni/Au ohmic contacts to p-type GaN", *Appl. Phys. Lett.* **76**, 3703 (2000).
17. A. Dmitriev and A. Oruzheinikov, "The rate of radiative recombination in nitride semiconductors and alloys", *J. Appl. Phys.* **86**, 3241 (1999).
18. H. Morkoç, S. Strite, G.B. Gao, M.E. Lin, B. Sverdlov, and M. Burns, "Large band-gap SiC, III-V nitrides, and II-VI ZnSe-based semiconductor device technologies", *J. Appl. Phys.* **76**, 1363 (1994).
19. E.S. Dettmer, B.M. Romensko, H.K. Charles, Jr., B.G. Carkhuff, and D.J. Merrill, "Steady state thermal conductivity measurements of AlN and SiC substrate materials", *IEEE Trans. Comput. Hybr. Manufact. Technol.* **12** 543 (1989).
20. W. Nakwaski, "Thermal conductivity of binary, ternary, and quaternary III-V compounds", *J. Appl. Phys.* **64**, 159 (1988).
21. Y.S. Touloukian, R.W. Powell, C.Y. Ho, and P.G. Klemens, *Thermophysical Properties of Matter* **1** and **2**, IFI/Plenum, New York 1970.
22. P.G. Eliseev, "Line shape function for semiconductor laser modelling", *Electron. Lett.* **33**, 2046 (1997).
23. H. Katoh, T. Takeuchi, C. Anbe, R. Mizumoto, S. Yamaguchi, C. Wetzel, H. Amano, I. Akasaki, Y. Kaneko, and N. Yamada, "GaN based laser diode with focused ion beam etched mirrors", *Jpn. J. Appl. Phys.* **37**, Pt. 2, L444 (1998).
24. T. Kuroda and A. Tackeuchi, "Free carrier screening of quantum-confined Stark effect affecting on luminescence energy shift and carrier lifetime in InGaN quantum wells", *Proc. Intern. Workshop on Nitride Semiconductors*, Nagoya, Japan, 24-27 Sept. 2000, IPAP Conf. Series **1** 516 (2000).
25. *Handbook of Optical Constants of Solids* **1** and **2**, Academic Press, Orlando 1985.
26. M.J. Bergmann and H.C. Casey, Jr., "Optical-field calculations for lossy multiple layer $Al_xGa_{1-x}N/In_xGa_{1-x}N$ laser diodes", *J. Appl. Phys.* **84**, 1196 (1998).